Research Article
Angewandte Chemie International Edition
www.angewandte.org
How to cite: *Angew. Chem. Int. Ed.* **2026**, *65*, e20124
doi.org/10.1002/anie.202520124

Environmental Risk Assessment | Hot Paper

Mapping Antibiotic Photocatalytic Transformation and Resistance Risks with a DFT-Informed Machine Learning Workflow

Chen-Chen Zhao, Sihan Xing, Cheng Fu, Lifeng Zheng, Huaizhu Wang, Zhong Jin, Shuhua Li, Shujuan Zhang, and Jing Ma**

Abstract: The photocatalytic degradation of antibiotics is effective but may yield transformation products (TPs) that sustain or amplify ecological risks, including antibiotic resistance gene (ARG) induction. This study developed a predictive framework that couples photocatalytic experiments, high-resolution mass spectrometry, density functional theory (DFT) calculations and machine learning (ML) to assess risks of TPs. Using tetracycline as a model compound, we constructed a reaction network over 120 steps and 9 533 reactions, and trained an ML model to rapidly predict Gibbs free energy changes with DFT accuracy. Automatic transition-state searches were integrated to evaluate kinetic accessibility within the network. The generalizability of this approach was validated with pathways of five different antibiotics involving 545 reactions. Furthermore, a multi-dimensional scoring system was developed that integrates diversity, ecotoxicity, biodegradability, and feasibility (DEBF) to prioritize pathways by both reactivity and sustainability. Several hydroxylated, aminated, and amide–ketone TPs were identified as high-risk species with enhanced ARG-binding potential. By bridging molecular energetics with ecological outcomes, this work offers a generalizable, mechanism-anchored, and risk-aware approach for analyzing photocatalytic transformations and deriving design principles for pollutant degradation that balance efficiency with ecological safety.

Introduction

The pervasive release of organic contaminants from pharmaceutical, agricultural, and industrial sources continues to challenge the integrity of global aquatic environments.[1,2] Among these, antibiotics are of particular concern. Their complex structures and environmental persistence, coupled with the potential for their transformation products (TPs) to promote antibiotic resistance and exert unknown toxicological effects, pose a significant threat to ecosystems and public health.[3,4] Advanced oxidation processes, particularly heterogeneous photocatalysis,[5,6] have emerged as a promising strategy for mitigating this pollution. By generating reactive oxygen species (ROS) under light irradiation, photocatalysis can degrade recalcitrant antibiotics efficiently and sustainably.[7,8] However, most existing studies have focused primarily on degradation efficiency, with limited understanding on the underlying degradation mechanisms and the environmental fate of TPs.

Recent advances in analytical and computational techniques have begun to address this complexity. The integration of high-resolution mass spectrometry (HRMS) with network-based approaches has enabled more comprehensive tracking of transformation pathways.[9–12] By leveraging data-driven algorithms, researchers have attempted to infer intermediate structures and predict their evolution, aiming to construct a transformation “trajectory map”.[13,14] However, the structural elucidation of TPs based on MS data remains a challenge. A single mass-to-charge (*m/z*) ratio may correspond to numerous structural isomers, leading to a combinatorial explosion of candidate structures.[15] This not only introduces ambiguity into structural identification but also increases the computational complexity of theoretical validation and pathway construction. In parallel, single-molecule sensing platforms have demonstrated the possibility of unambiguous structural discrimination in other fields. For example, nanopore-based approaches can resolve amino acids and their post-translational modifications at the single-molecule level,[16] but not yet broadly applicable to the contaminants encountered in aquatic environments. Moreover, from a mechanistic perspective, photocatalytic oxidation of structurally complex compounds such as antibiotics may proceed through other routes beyond classical cleavage and mineralization. Radical-driven rearrangements and intermolecular coupling reactions can also occur, giving rise to oxidation–polymerization pathways that generate stable, poorly degradable, and potentially toxic oligomeric products.[17–20] Such outcomes complicate the interpretation

---

[*] C.-C. Zhao, S. Xing, C. Fu, L. Zheng, H. Wang, Prof. Dr. Z. Jin, Prof. Dr. S. Li, Prof. Dr. J. Ma
State Key Laboratory of Coordination Chemistry, School of Chemistry, Nanjing University, Nanjing, Jiangsu 210023, P.R. China
E-mail: majing@nju.edu.cn

Prof. Dr. S. Zhang
State Key Laboratory of Water Pollution Control and Green Resource Recycling, School of Environment, Nanjing University, Nanjing, Jiangsu 210023, P.R. China
E-mail: sjzhang@nju.edu.cn

Additional supporting information can be found online in the Supporting Information section

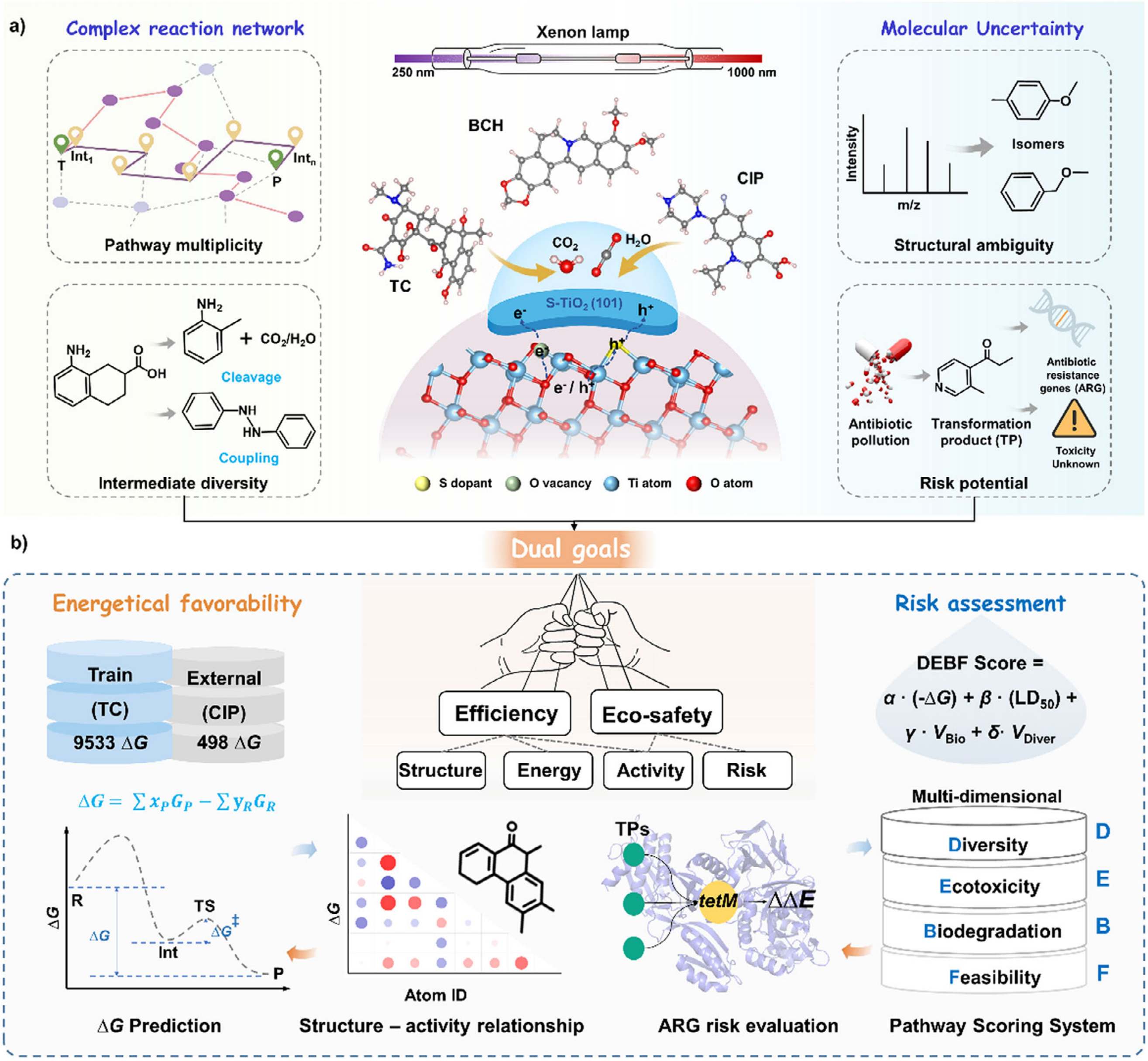

Figure 1. Automatic workflow for mechanism-informed and risk-aware assessment of photocatalytic antibiotic degradation. a) Mechanistic complexity and molecular uncertainty in antibiotic degradation. b) Predictive framework integrating reaction energy evaluation and eco-risk scoring.

of degradation processes and challenge the prevailing assumption that more complete degradation necessarily equates to greater safety. These situations highlight the urgent need for new strategies capable of capturing the full diversity of transformation pathways and assessing the environmental risks in a fast and predictive manner.

To address this challenge, a mechanism-informed and risk-aware automatic workflow was developed to evaluate the photocatalytic transformation of antibiotics using visible-light-driven S-doped TiO_2 catalyst (Figure 1). By combining photodegradation experimental, HRMS and LC-MS analysis, density functional theory (DFT) calculations and transition state explorations, the dominant ROS and key TPs were firstly identified. We then constructed a massive, detailed reaction network for tetracycline (TC) comprising over 9000 reactions. To overcome the computational bottleneck of evaluating such a network, we employed machine learning (ML) models trained on DFT data to rapidly predict the thermodynamic feasibility (ΔG) of each step, enabling the large-scale, network-wide assessment of photocatalytic pathways. We also developed a multi-dimensional informative scoring system (DEBF) that integrates diversity, ecotoxicity, biodegradability, and feasibility of pathway to prioritize optimal transformation routes that balance efficiency with sustainability. Finally, we quantified a critical but often overlooked risk: the potential for TPs to induce antibiotic resistance. Through molecular docking simulations against the *tetM* protein, we found that several TPs could strongly interact with key active site residues, suggesting a possible mechanism for enhanced antibiotic resistance gene (ARG) binding tendencies. By bridging molecular structure, reaction energetics, transformation diversity, and ecological risk, this study not only deepens the mechanistic understanding of photocatalytic antibiotic degradation but also establishes a generalizable methodology for screening safer and more sustainable water treatment processes.

Results and Discussion

Reactive Species Identification

Advances in catalyst design, including heterojunction engineering,[5,6] oxygen vacancy modulation,[21,22] and single-atom catalysis,[23] have significantly enhanced the yield and selectivity of ROS. Inspired by our previous finding[21] that sulfur doping and oxygen vacancies in TiO_2 (S-TiO_2) promoted the activation of inert N—N triple bonds, we suggest that antibiotics rich in reactive groups (e.g., amino substituents) might undergo more efficient degradation on such catalysts. The S-TiO_2 photocatalyst used herein was synthesized following our previously reported method[21] where comprehensive structural and electronic characterizations (e.g., X-ray photoelectron spectroscopy, UV–vis diffuse reflectance spectroscopy, valence band XPS, and electrochemical impedance spectroscopy) displayed successful S-incorporation, narrowed band gap, and enhanced charge separation. Accordingly, the photocatalytic performance of S-TiO_2 toward three antibiotics, tetracycline (TC), ciprofloxacin (CIP), and berberine chloride hydrate (BCH), was systematically evaluated under visible light (Figure 2a). Rapid photocatalytic removal of the antibiotics was observed, with efficiencies of TC (98.99%), CIP (94.59%) and BCH (99.66%) after 180 min. The degradation followed pseudo-first-order kinetics (Figure 2b), with BCH showing the highest rate constant ($k = 0.0333\ \text{min}^{-1}$), consistent with its superior removal efficiency. As shown in Figure 2c, the electron paramagnetic resonance (EPR) spectra confirmed the formation of multiple reactive species during irradiation, including singlet oxygen ($^1O_2$), superoxide radical ($O_2^{\bullet -}$), hydroxyl radical (·OH) and photogenerated electron (e^-). The photocatalytic mechanism was proposed in Figure 2d. Upon light excitation, S-TiO_2 generates electron–hole pairs. The photoexcited electrons reduce molecular oxygen (O_2) to $O_2^{\bullet -}$. Given the relatively low valence band potential (+0.66 V versus NHE), direct oxidation of water or surface hydroxyl groups to produce ·OH is thermodynamically unfavorable. Instead, ·OH generation likely proceeds via an indirect pathway involving a series of chain reactions. Specifically, $O_2^{\bullet -}$ can react with protons to form hydroperoxyl radical (•HO_2), which further converts into hydrogen peroxide (H_2O_2). The subsequent decomposition of H_2O_2 under light irradiation then yields ·OH.

The contributions of individual ROS were investigated using selective radical scavengers.[24] As illustrated in Figure 2e, the degradation of antibiotics under visible light was significantly influenced by the addition of selective scavengers (detailed results shown in Supporting Section 2 and Figure S1). For CIP, the nearly identical effects of $\cdot OH_{total}$ ((including surface-adsorbed and free hydroxyl radicals) and $\cdot OH_{free}$ (free hydroxyl radicals in solution), together with $O_2^{\bullet -}$, indicated that these were the primary oxidants, while the role of photogenerated hole (h^+) was negligible. In the case of TC, $O_2^{\bullet -}$ and h^+ dominated the degradation, whereas $\cdot OH_{free}$ contributed only marginally. For BCH, both h^+ and $O_2^{\bullet -}$ were the main contributors, followed by ·OH. These differences can be rationalized by structural characteristics: TC contains multiple hydroxyl and amino substituents prone to electrophilic attack, making ·OH less critical compared to charge-transfer pathways; CIP, with a quinolone core and an electron-withdrawing fluorine substituent, is more susceptible to oxidation driven by ·OH and $O_2^{\bullet -}$ but resists hole oxidation; and BCH, as a quaternary ammonium alkaloid with a planar aromatic skeleton, strongly adsorbs on the catalyst surface and undergoes charge-transfer processes, explaining its stronger dependence on h^+ and $O_2^{\bullet -}$. These structure–activity relationships highlight how intrinsic molecular features dictate the predominant ROS pathways during photocatalytic degradation, which is in line with the subsequent atomic-level analysis of reactive sites.

Thermodynamic and Kinetic Feasibility Screening

Liquid chromatography–mass spectrometry (LC–MS) (Figure S2) and HRMS (Figure S3) were employed to detect TPs and clarify the photocatalytic degradation mechanism of antibiotics over S-TiO_2. TC was selected as a representative compound for detailed analysis. The detected TPs, with their elemental composition, molecular formulas, DFT-calculated chemical structures and energies, are summarized in Table S3. Based on the LC–MS results and the temporal evolution of peak intensities of the detected TPs (Figures S4, S5), five plausible degradation pathways (Pathways I–V) were proposed (Figure 3a), involving key processes such as demethylation, hydroxylation, ring opening, and functional group cleavage. The corresponding reaction energetics are summarized in Table S4 (detailed thermodynamic evaluation method is presented below).

The apparently large ΔG magnitudes are caused by the expression of those reaction equations in overall stoichiometric transformations involving multiple small molecules (e.g., O_2, H_2O, CO_2, NH_4^+, and NO_3^-), rather than single elementary steps. Each reaction represents the net oxidation of complex intermediates to more mineralized products under photocatalytic conditions. The detailed rationale for these values is provided and further discussed in latter sections. These observations not only pinpoint the reactive atomic sites and structural motifs prone to degradation but also provide experimental support for the subsequent theoretical calculations of site reactivity and pathway feasibility.

A reaction network was constructed to integrate the experimentally identified TPs with five different reaction types (H-abstraction, radical recombination, ring opening, fragment eliminations, and multi-electron oxidations) and energetics (Figure 3b). In this network, nodes denote TC and the detected TPs, whereas edges represent individual transformation steps connecting $TP_i \rightarrow TP_j$. Edge colors

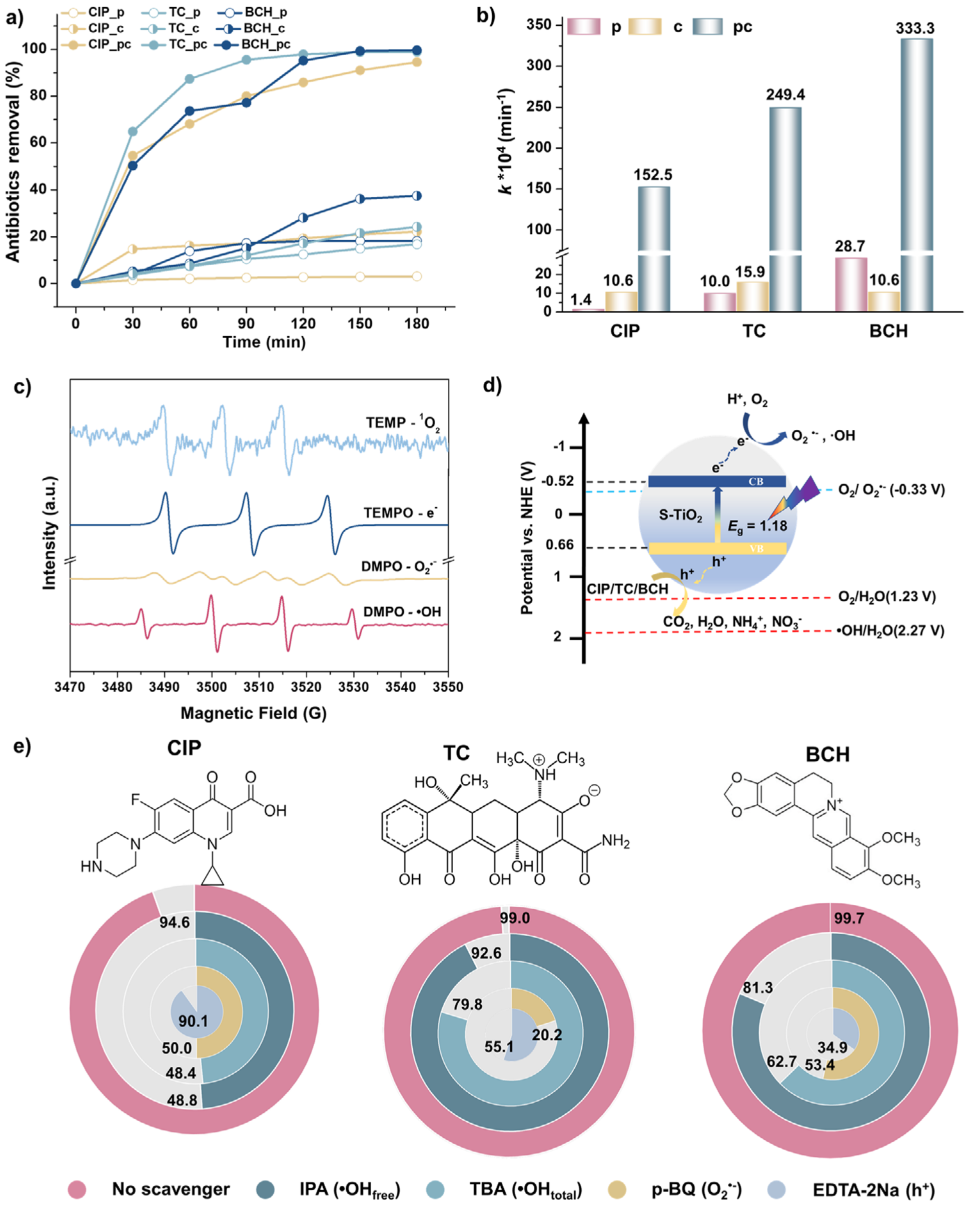

Figure 2. Photocatalytic degradation performance and reactive species identification of three antibiotics (TC, CIP, and BCH) over S-TiO$_2$ (1 g·L^{-1}) under visible light (300 W Xe lamp, 238 mW·cm^{-2}). a) Degradation efficiency of three kinds of antibiotics (CIP, TC, BCH) under different conditions: photocatalysis (pc), light-only (p), and catalyst-only (c) over 180 min. b) Reaction rate constants (k) derived from pseudo-first-order fitting. c) EPR spectra showing the generation of reactive species under visible light. d) Proposed photocatalytic mechanism of S-TiO$_2$ under visible-light irradiation. e) Structure of antibiotics and relative contributions of reactive species to the quenching experiments after 180 min using various scavengers: tert-butanol (TBA, ·OH$_{total}$), isopropanol (IPA, ·OH$_{free}$), p-benzoquinone (p-BQ, $O_2^{\cdot-}$), and ethylenediaminetetraacetic acid disodium salt (EDTA-2Na, h$^+$) with each antibiotics.

encode reaction classes. The network topology highlights several highly connected intermediates (hub TPs) that bridge multiple reaction classes and act as branching points linking different degradation routes, consistent with the pathway assignments in Figure 3a.

In total, 2 452 intermediates and 1 450 transition states (TSs) were located. Transition states searches and activation free energy barriers ($\Delta G^{\ddagger}$) calculations were performed using the automated design of chemical reactions (ADCR)[25] framework (see Supporting Section 3.6, Figures 4 and S7–S11). This TS search methodology has been widely applied to a broad variety of reaction types.[26–34] After the rapid reaction pathway searches at the GFN2-xTB level, the activation free energies barriers ($\Delta G^{\ddagger}$) were then benchmarked against M06-2X/6–311 + G(d,p), with the details shown in the Supporting Information (Figure S6 and Tables S5, S6). Based on 108 benchmark data at M06-2X level, the linear or non-linear regression relations were gained between the M06-2X and GFN2-xTB results with relatively high correlation coefficients ($R^2 >$ 0.91). Then GFN2-xTB free energies were corrected to approach M06-2X accuracy using the relatively simpler linear regression equation. It should be

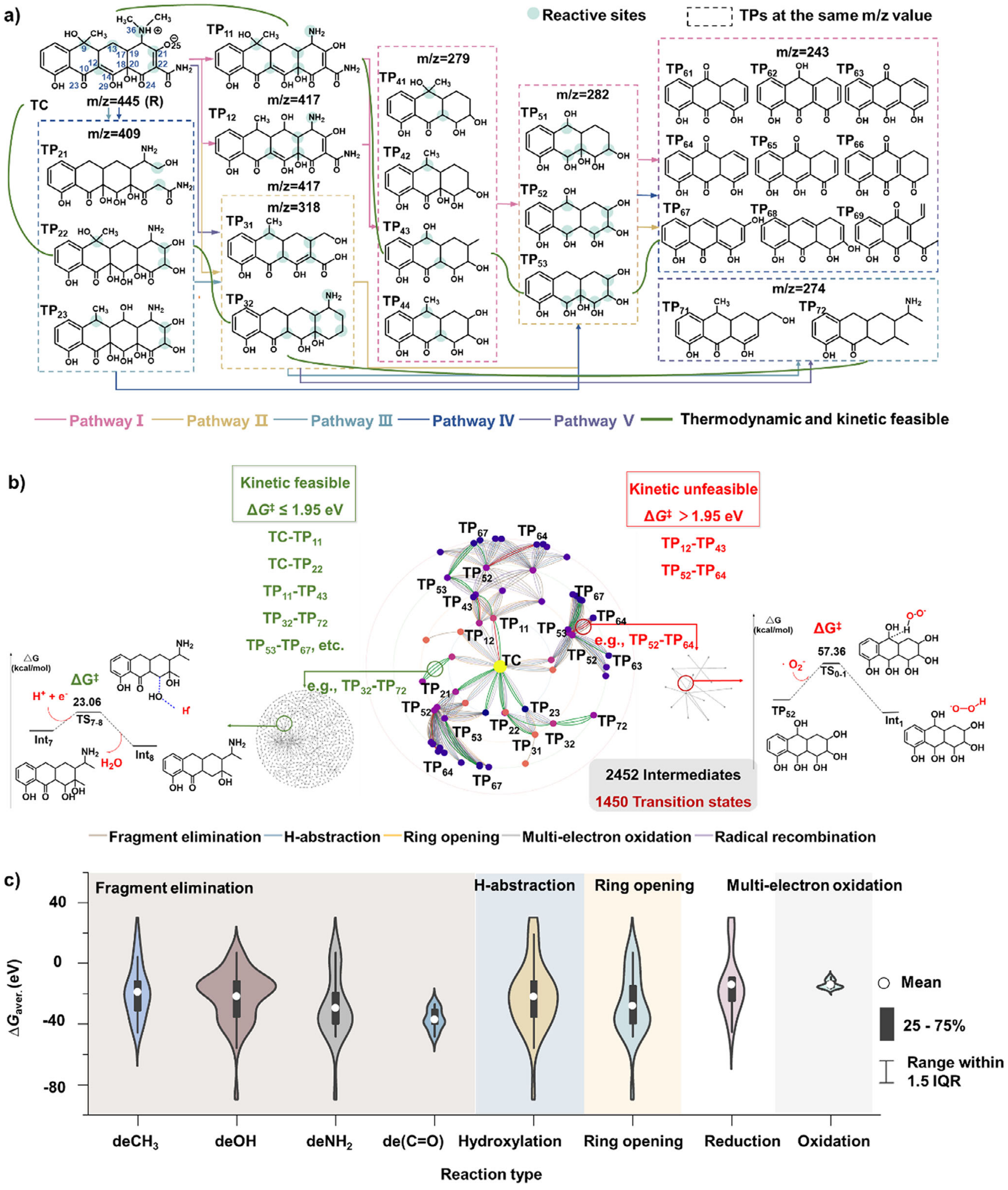

Figure 3. Possible degradation pathways and reaction energetics of TC over S-TiO_2. a) Transformation products (TPs) identified by LC–MS and the proposed five degradation pathways (Pathway I–V). b) Reaction network of TC degradation, where nodes denote TC/TPs and edges are colored by reaction class and annotated by DFT-derived kinetic descriptors. c) Statistical distribution of reaction free energies (ΔG) for key reaction types, including demethylation ($deCH_3$), dehydroxylation (deOH), deamination ($deNH_2$), decarbonylation (de(C=O)), hydroxylation, ring opening, reduction of carbonyl and oxidation of alcohol to aldehyde.

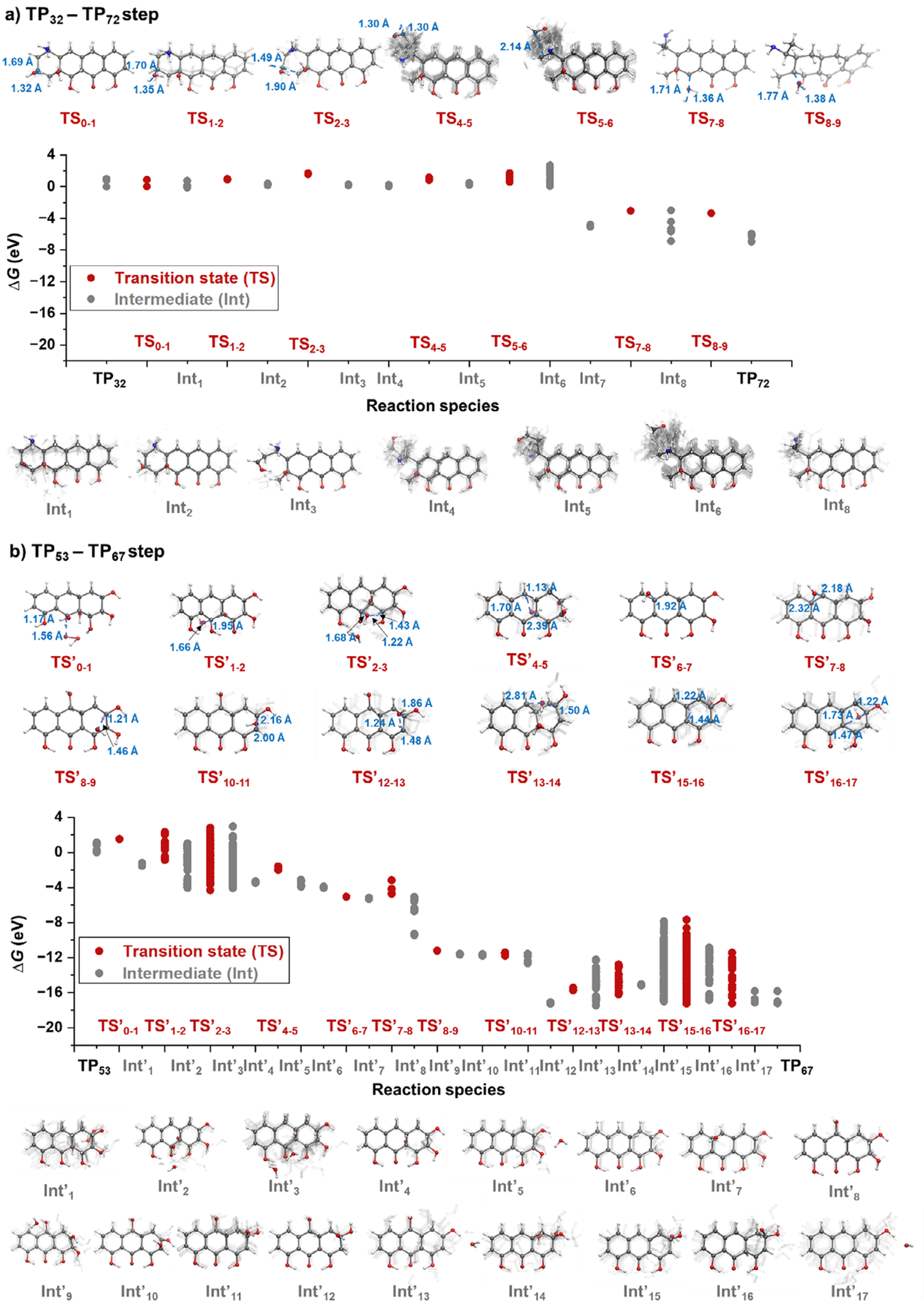

Figure 4. Illustration of kinetic feasibility analysis of two reaction steps: a) TP$_{32}$–TP$_{72}$ and b) TP$_{53}$–TP$_{67}$ among the studied seven reaction paths (displayed in supporting information) to show the automated searched reaction transition states (in red) and intermediates (with the superimposed structures up to 40 conformations). Key bond lengths involved in TSs are in units of angstroms, Å.

mentioned that the good correlation of the simple DFT-xTB regression equation for energy correction is probably due to its application in a very limited scope of reaction pathways generated in this work. For more general applications to other reactions of various organic molecules, further improvements in narrowing DFT-xTB gap could be implemented by using neural-network machine learning potentials, as reported in some recent literatures.[35,36]

The present workflow is useful to qualitatively rank kinetic accessibility. Based on the resulting $\Delta G^{\ddagger}$ information, the combination of thermodynamic–kinetic pathway feasibility was evaluated for seven important branching transformations ($TC–TP_{11}$, $TC–TP_{22}$, $TP_{12}–TP_{43}$, $TP_{22}–TP_{32}$, $TP_{52}–TP_{64}$, $TP_{53}–TP_{67}$, and $TP_{32}–TP_{72}$). The related results were given in Figures 3b, 4, and S7–S11. Green edges denote transformations with moderate barriers ($\Delta G^{\ddagger} \leq 1.95$ eV), such as $TC\text{-}TP_{11}$, $TC\text{-}TP_{22}$, $TP_{32}\text{-}TP_{72}$, which are considered kinetically feasible under photocatalytic conditions. Red edges indicate steps with higher barriers ($\Delta G^{\ddagger} > 1.95$ eV), like $TP_{12}\text{-}TP_{43}$, $TP_{52}\text{-}TP_{64}$, that are likely kinetically hindered. By jointly considering thermodynamic driving forces and kinetic accessibility, we recommend several feasible degradation routes, including $TC \rightarrow TP_{11} \rightarrow TP_{43} \rightarrow TP_{53} \rightarrow TP_{67}$ in path I, and $TC \rightarrow TP_{22} \rightarrow TP_{32} \rightarrow TP_{72}$ in path III (highlighted in green trajectories in Figure 3a).

A closer inspection of the TPs revealed that the two rings on the left side of the TC scaffold remained largely intact, indicating their relative inertness. In contrast, the right-hand rings underwent extensive transformations. Beyond this global landscape, statistical analysis (Figure 3c) showed that fragment eliminations, including demethylation ($deCH_3$), dehydroxylation (deOH), deamination ($deNH_2$), decarbonylation (de(C═O)), hydroxylation, ring opening, reduction and multi-electron oxidations occurred across the five pathways. The average Gibbs free energy changes ($\Delta G_{\text{aver.}}$) of these processes were calculated. The frequency of "deOH" and hydroxylation across multiple routes underscores their central role in driving molecular diversification. Thermodynamically, the most favorable steps included "de(C═O)" ($\Delta G_{\text{aver.}} = -37.2$ eV), "$deNH_2$" ($\Delta G_{\text{aver.}} = -29.6$ eV, and ring opening ($\Delta G_{\text{aver.}} = -28.1$ eV), suggesting that specific atomic sites such as C(9), C(13), C(19), C(20), C(22), O(24), and N(36) are preferentially attacked by ROS.

Among the studied seven kinetic pathways, two key transformations ($TP_{32}–TP_{72}$ and $TP_{53}–TP_{67}$) were selected in Figure 4 to display the complete multistep profile, including all intermediates and TSs along the reaction coordinate. The energy profiles of all the other transformation steps are given in Figures S7–S11. As shown in Figure 4, the superimposed structures of intermediates (Ints) and TSs are presented, with key bond lengths involved in bond-breaking and bond-forming steps annotated in angstroms (Å). Full reaction profiles and optimized structures for the $TP_{32}–TP_{72}$ pathway are provided in Figure S7. The calculated activation free energy barriers for generating TSs generally range from 0.43–1.95 eV (10–45 kcal mol^{-1}). For instance, the rate-determining step in the $TP_{32}–TP_{72}$ conversion involves ring-opening ($Int_2\text{-}Int_3$) and formaldehyde elimination ($Int_5\text{-}Int_6$) steps, suggesting that the elementary steps are kinetically feasible under photocatalytic conditions. In addition, radical-mediated reactions such as hydrogen abstraction ($TP_{32} - Int_1$) and hydroxyl group elimination ($Int_7 - Int_8$ and $Int_8 - TP_{72}$) showed even lower barriers (<1.08 eV (25 kcal mol^{-1}), suggesting that once the corresponding radicals are formed, downstream transformations can proceed efficiently.

Prediction of Reaction Feasibility (ΔG)

To accelerate thermodynamic screening across this complex degradation network, ML models were developed to predict ΔG. A dataset of 9 533 DFT-calculated ΔG values was constructed, covering 120 overall degradation reactions and 9 533 reaction steps. Each step describes the transformation of TPs via environmental species (O_2, H_2O, and pH conditions), ROS ($^1O_2$, $O_2^{\cdot-}$ and ·OH) or photogenerated charge carriers (e^-, h^+). These reactions typically lead to mineralized products such as CO_2, H_2O, NH_4^+, and NO_3^- (Figure 5a). The ΔG distribution across the full degradation network is presented in Table S4, some of which were benchmarked against the different DFT level, ωB97X-D/def2-TZVP, in Figure S12a–b. Furthermore, by modeling tetracycline adsorption on the S–TiO_2 surface (Figure S12c) and sampling explicit water–intermediate configurations (21 conformations for Int'5a–u and 31 for Int'17a–af, Figure S12d), we found stable chemisorbed structures with comparable binding energies and reaction profiles, indicating that interfacial interactions and explicit solvation do not alter the trends in relative reaction free energy changes.

Because the original ΔG values span a wide range, all values were normalized by min–max scaling to the [0, 1] range before ML training. The resulting dimensionless quantity, denoted as ΔG_{norm}, was used for both model input and evaluation to ensure numerical stability and to prevent large-magnitude reactions from the regression process (details given in Supporting Information, Section 1.7).

A total of 16 molecular and reaction descriptors were initially extracted for each step, including stoichiometric coefficients of reactants or products (x/y), and orbital-energy descriptors such as energy of the highest occupied molecular orbital (E_{HOMO}), and their difference ($\Delta E_{\text{H-L}}$) (Detailed feature engineering is described in Supporting Information, Section 3.8). Taking the following reaction as an example:

$$C_{22}H_{24}N_2O_8 + 4O_2^{\cdot-} + 4H^+ = C_{20}H_{20}N_2O_8 + 2CO_2 + 4H_2O \quad (1)$$

Therein, the stoichiometric numbers for the reactants are $x(C_{22}H_{24}N_2O_8$, denoted as $TP_i) = -1$, $x(O_2^{\cdot-}) = -4$, $x(H^+) = -4$, while the products are $y(C_{20}H_{20}N_2O_8$, denoted as $TP_j) = 1$, $y(CO_2) = 2$, $y(H_2O) = 4$. Orbital-related molecular features include E_{HOMO}, and $\Delta E_{\text{H-L}}$ for both reactants (TP_i) and products (TP_j).

The H_2O normally appears as a product, but if H_2O participates as a reactant, its stoichiometric number is taken as negative. For example:

$$C_{15}H_{18}O_5 + 6h^+ + 3H_2O = C_{14}H_{18}O_6 + CO_2 + 6H^+ \quad (2)$$

Here, $y(H_2O) = -3$.

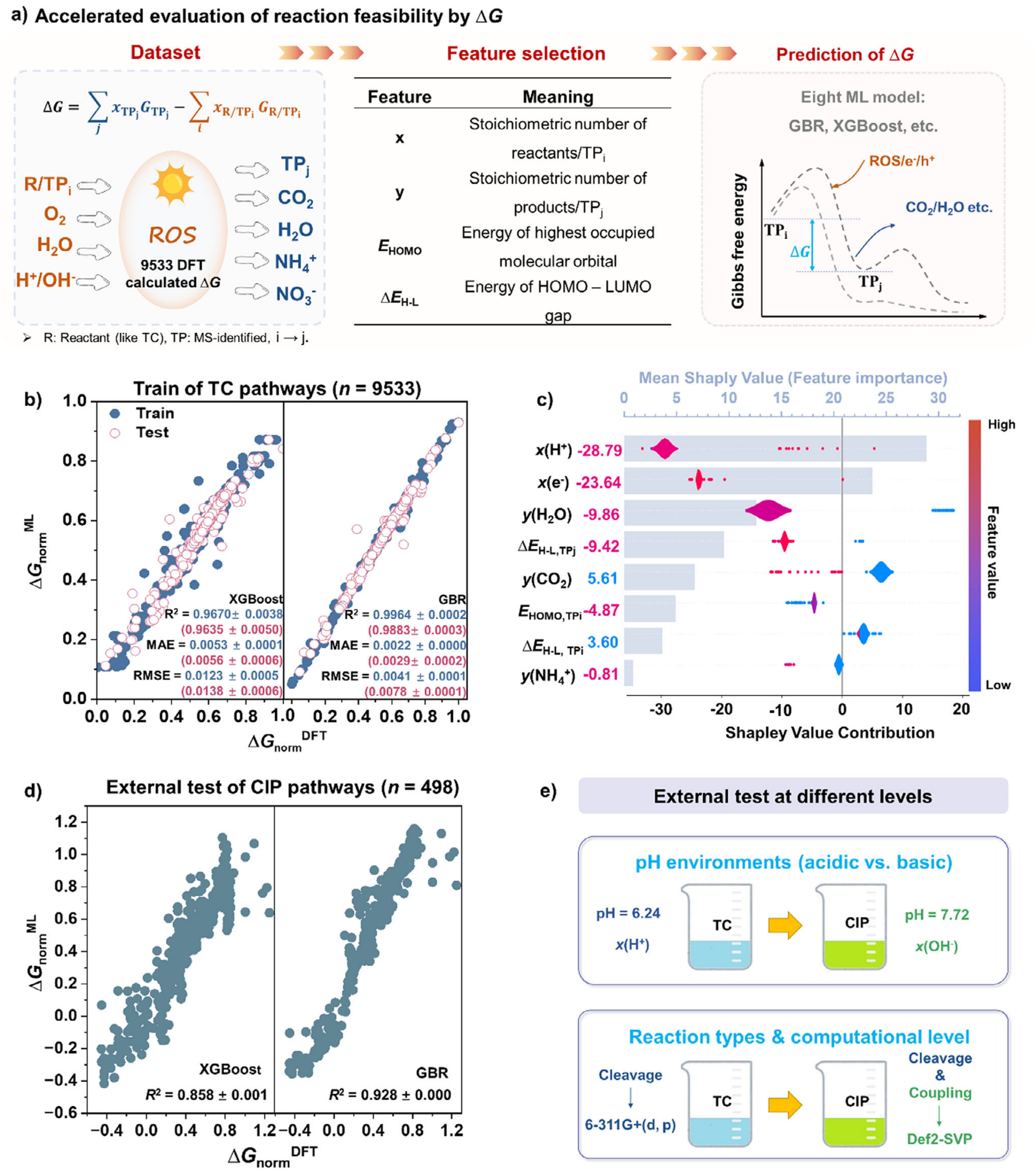

Figure 5. Machine learning prediction of Gibbs free energy changes across antibiotic degradation networks. a) Construction of the reaction database and extraction of molecular/reaction descriptors for ML model input. b) Correlation of the DFT-calculated normalized free energy changes, ΔG_{norm}, (by min–max scaling to the [0,1] range) with ML predicted from different models under 5-fold cross-validation. c) Feature importance analysis (SHAP values) highlighting the most influential descriptors. d) External validation of CIP degradation pathways. e) Robust model performance under varied conditions (pH environments, reaction types, and computational levels).

We systematically reduce the descriptors number from 16 to 12, 8, 6, and finally 4 (Table S7), to see the variation in ML model performance. Feature selection ultimately identified an optimal subset of eight descriptors ($x(\mathrm{H}^+)$, $x(\mathrm{e}^-)$, $y(\mathrm{NH_4}^+)$, $y(\mathrm{CO_2})$, $y(\mathrm{H_2O})$, $E_{\mathrm{HOMO,TPi}}$, $\Delta E_{\mathrm{H\text{-}L,TPi}}$ and $\Delta E_{\mathrm{H\text{-}L,TPj}}$). Using these features, various ML algorithms with 5-fold cross-validation were trained (see Supporting Section 1.7, Section 3.9, Figures S13 and S14 for model performance comparison), with XGBoost and gradient boosting regression (GBR) achieving the best performance (RMSE = 0.0138 eV/0.0078 eV, MAE = 0.0056 eV/0.0029 eV and R^2 = 0.9635/0.9883 in the test, respectively) (Figure 5b). For reference and easy back-mapping, model performances based on unnormalized ΔG values are also provided in Figure S15. Feature importance analysis (Figure 5c, correlation analysis shown in Figure S16) confirmed that constant of $x(\mathrm{H}^+)$ and $x(\mathrm{e}^-)$ were the most influential, followed by the water constant $y(\mathrm{H_2O})$. The $\Delta E_{\mathrm{H\text{-}L}}$ also contributed significantly to the model's predictive capability. The model successfully captured key trends and was sufficient for pathway prioritization and reaction feasibility screening.

To evaluate model robustness, we conducted comprehensive error diagnostics based on out-of-fold (OOF) predictions from 5-fold cross-validation. As detailed in Section 3.10 and Figures S17–S20, the residuals ($\Delta G'$) between predicted and DFT-calculated Gibbs free energy values for the GBR model are symmetrically distributed around zero, variance is homoscedastic across the $\Delta G'$ range, residuals follow an approximately Gaussian distribution, and prediction errors do not increase with $|\Delta G'|$. These results confirm the accuracy, bias-free nature, and scale-invariance of the GBR model.

External test was performed using five other antibiotics beyond TC, including ciprofloxacin (CIP), sulfathiazole, metronidazole, linezolid, and polymyxin G (Supporting Section 3.11). Among them, the degradation pathway of CIP was obtained experimentally in this study, while the other four were extracted from literature reports.[37–40] In total, 545 reactions were used for validation, with the external validation results summarized in Figure S21. As a representative system, CIP was used to illustrate the performance of the ML model (Figure 5d, LC–MS spectra and structures of TPs during CIP degradation are shown in Figures S22 and S23 and Table S8). The ΔG values predicted by the ML model exhibited good agreement with DFT calculations in all the selected systems, demonstrating the generalizability of the model across structurally diverse antibiotic systems. Notably, the photocatalytic degradation of CIP did not proceed through a single mineralization pathway but rather a multi-pathway regime involving cleavage and coupling. Such complexity highlights the important implications (Figure 5e): i) TC is typically dissolved under acidic conditions, so H^+ ions were incorporated into the photocatalytic degradation equations. When CIP (with a solution pH of 7.76) was used as an external validation set, the corresponding OH^- replaced H^+ in the descriptors. Remarkably, the TC-trained model still yielded accurate ΔG predictions for CIP, indicating its adaptability to different pH conditions, ii) the training set consisted predominantly of bond cleavage reactions, yet the model is successfully generalized to external validation data that also included bond-forming (coupling) processes, again producing reliable predictions, and iii) even when reactions were calculated at different computational levels, for example, cleavage steps with the 6–311G+(d,p) basis set versus coupling processes with the def2-SVP basis set, the model maintained high predictive accuracy. These examples collectively demonstrate that the model can robustly capture reaction energetics across diverse degradation scenarios.

Interpretability of the Prediction Model

The earlier analyses of antibiotic structures already hinted at an uneven landscape of reactivity, some rings appeared remarkably inert, while others were repeatedly attacked, and small substituents such as amino or hydroxyl groups seemed especially labile. To move from these qualitative observations to a quantitative, atom-level understanding, we asked: which atoms are truly the "hot spots" of degradation, and why? The atom-level degradability analysis was performed by integrating pollutant electronic structures with thermodynamic calculations and structure–reactivity modeling. In this study, we assumed that ΔG associated with radical attack at a specific atomic site can serve as a reactivity indicator, with more negative ΔG values corresponding to higher susceptibility.

For TC, the optimized zwitterionic form (z-$\mathrm{TC}^{+/-}$, dominant at pH = 6.24 based on pK_a analysis) were analyzed, and its key structural and electronic parameters, including bond lengths, bond dissociation energies, Hirshfeld atomic charges, condensed Fukui functions, and condensed dual descriptors (CDD) were extracted in Figure 6a and Table S9. The atomic features in Figure 6b were used to train sure independence screening and sparsifying operato (SISSO) models[41] for five distinct reactive species ($\cdot\mathrm{OH}$, $\mathrm{O_2}^{\bullet-}$, $^1\mathrm{O_2}$, h^+, e^-). Separate linear models were developed to predict ΔG values and the fitted SISSO expressions are provided in Table S10.

To ensure comparability across different radicals, the normalized degradation scores were visualized in a "reactivity heatmap" (Figure 6c). The construction process of the antibiotic structure–degradability site association model is provided in the Supporting Section 4.3 (Table S11 and Figure S24). Each block represents the relative reactivity of an atom–radical pair, with red indicating higher susceptibility, and hierarchical clustering was applied to group atoms with similar response patterns. For example, atoms C(9), C(12), C(14), C(19), and N(36) consistently exhibited high degradation scores under multiple ROS, suggesting that they form a group of preferential degradation hotspots, likely due to localized electron density or inductive effects from neighboring groups. $\cdot\mathrm{OH}$ and e^- displayed statistically similar site preferences, dominated by N(36), though their mechanistic modes differ (electrophilic versus nucleophilic). In contrast, $^1\mathrm{O_2}$ and $\mathrm{O_2}^{\bullet-}$ clustered together, preferring conjugated or heteroatom-rich regions, while h^+ displayed more selective and structure-dependent responses. Importantly, $^1\mathrm{O_2}$, $\mathrm{O_2}^{\bullet-}$, and h^+ displayed multi-site activity, consistent with Fukui and CDD analyses showing that multiple atoms are simultaneously sensitive to electrophilic (e.g., h^+, $^1\mathrm{O_2}$) or nucleophilic (e.g.,

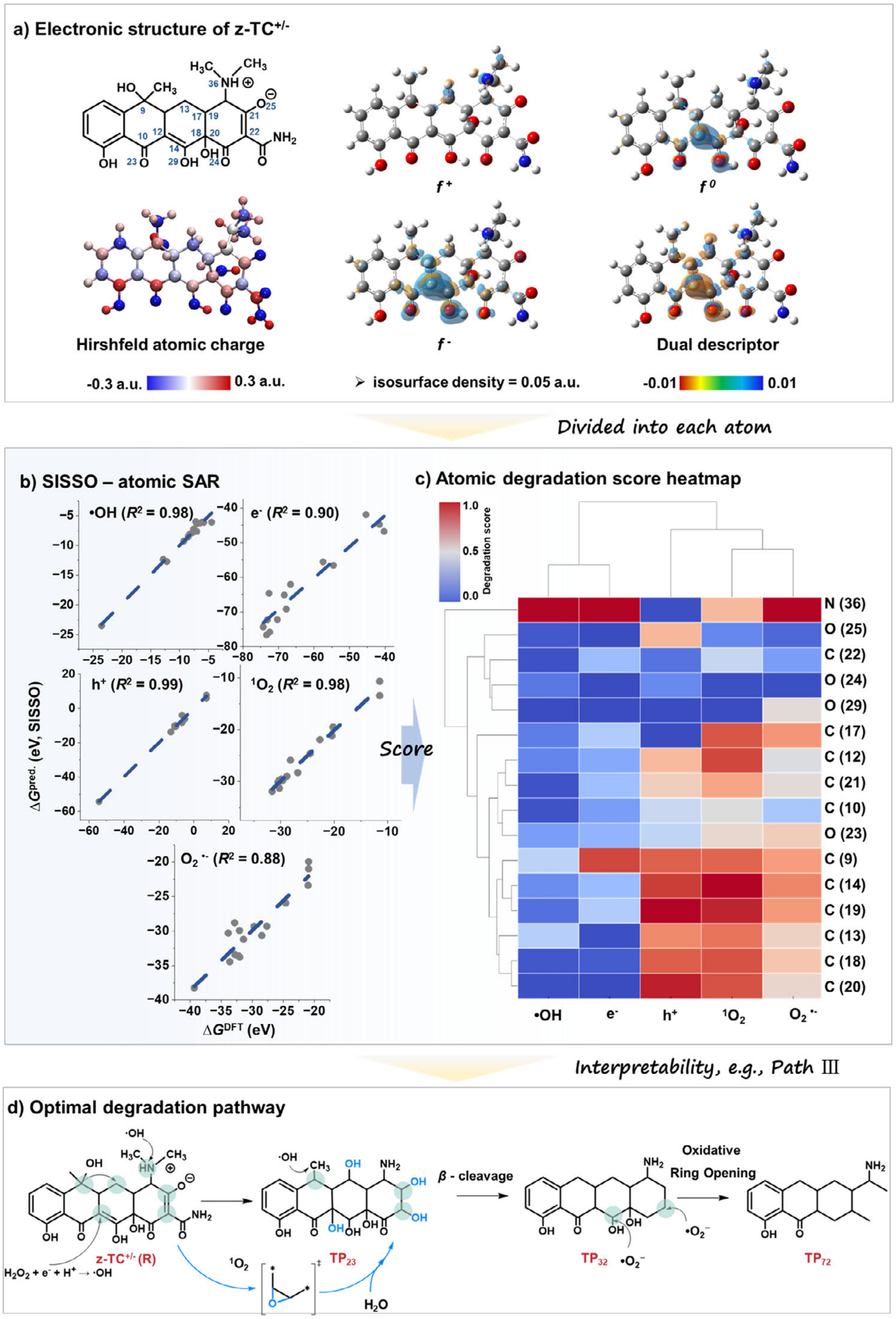

Figure 6. Atom-level degradability analysis of tetracycline based on electronic structure and radical response modeling. a) Electronic structure of the optimized zwitterionic tetracycline (z-TC$^{+/-}$) (iso-surface density = 0.05). The blue and orange colors represent the negative and positive phases of the molecular orbital. b) SISSO model prediction of ΔG for atom-specific radical attack. c) Multi-radical response heatmap showing normalized degradation scores and hierarchical clustering of atomic sites. d) Representative degradation pathway of TC.

$O_2^{\bullet -}$) attack. This highlights the strong adaptability of TC's electronic structure toward diverse oxidative environments.

By integrating the radical response heatmap with thermodynamic analysis, a representative degradation pathway was constructed (Figure 6d). Free energy calculations confirmed its strong thermodynamic driving force. The N(36) site showed high reactivity toward both ·OH and e$^-$, suggesting that the amino group is a primary initiation site. Subsequent α-C bond cleavage at C(9) facilitated skeleton dissociation, while $O_2^{\bullet -}$ and e$^-$ cooperatively generated H_2O_2, which decomposed to ·OH for further attack at C(12)/C(13). $^1O_2$ reacted with the C(21) = C(22) double bond to form an

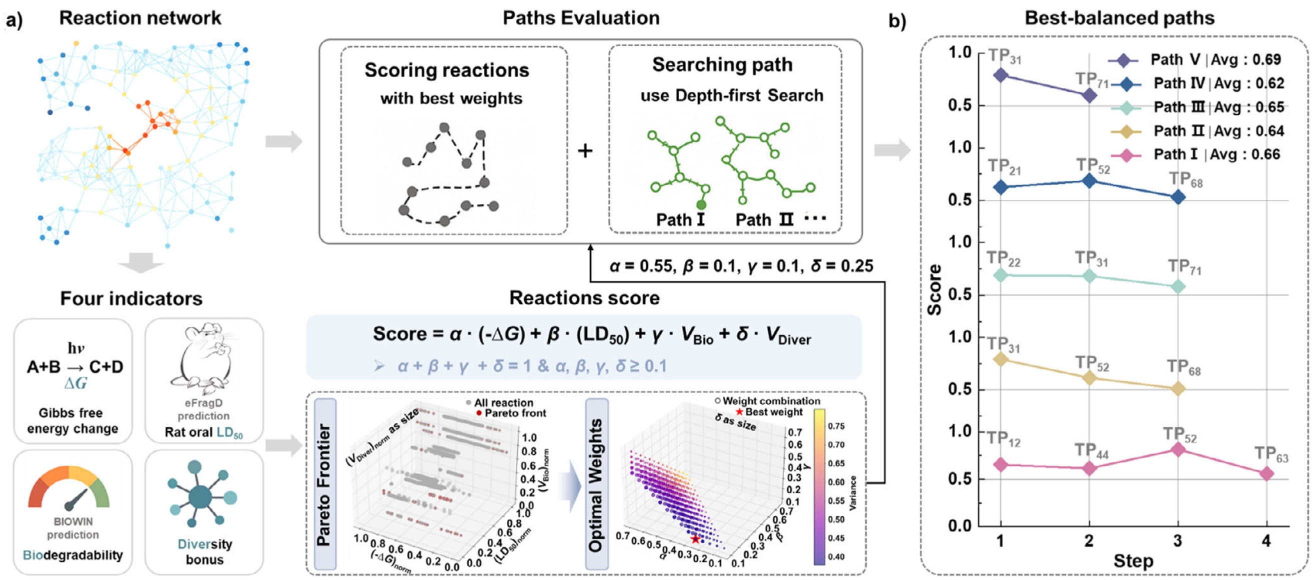

Figure 7. Evaluation framework for prioritizing environmentally favorable antibiotic degradation pathways. a) Systematic scoring workflow. b) Final optimal degradation routes proposed for five pathways.

epoxide that hydrolyzed into hydroxylated intermediates. Finally, β-scission and oxidative cleavage at C(20)/C(22) under h^+, $O_2^{\bullet -}$, or $^1O_2$ attack resulted in deep oxidation and ring opening.

Overall, this multi-species structure–activity profiling provides atom-level insight into site-specific reactivity under photocatalytic conditions. The strong agreement between electronic descriptors, radical response clustering, and thermodynamic pathways validates the predictive capability of the model, highlighting that degradation susceptibility is not uniformly distributed but governed by local electronic properties such as charge localization, Fukui indices, and bond energies.

Diversity–Ecotoxicity–Biodegradability–Feasibility (DEBF) Evaluation

TPs generated from different parent antibiotics may result in a diverse mixture, potentially leading to environmental accumulation and persistence. Toxicity prediction (rat oral LD_{50} predicted by eFragD method developed in our group) results (Figure S25) revealed that some TPs exhibited even higher toxicity than their parent compounds. This raises the need for assessing not only the reactivity of degradation steps but also the environmental fate of their TPs.

To systematically evaluate complex biodegradation networks and identify environmentally friendly degradation routes, we developed a scoring framework that integrates diversity, ecotoxicity, biodegradability, and feasibility of pathway (DEBF) into a unified decision process (Figure 7). Each reaction step was characterized by four descriptors (shown in Figure 7a): 1) reactivity feasibility (ΔG), employed as an indicator of degradation efficiency, 2) the acute toxicity of the TPs (LD_{50}), used as a proxy for eco-safety, 3) a biodegradability value (V_{Bio}) (detailed biodegradability data listed in Table S12) derived from the sum of four sub-models (BIOWIN 2, 3, 5, and 6) within the EPI Suite,[42] capturing biodegradability, and 4) a diversity bonus ($V_{\mathrm{Diver}} = \frac{1}{\sqrt{n}}$, where n is the number of times a product appears within the same step of a pathway), penalizing redundant intermediates and encouraging structural variation. All variables were normalized, and reaction score (0–1) was calculated using a weighted linear model:

$$\mathrm{Score} = \alpha \cdot (-\Delta G) + \beta \cdot (\mathrm{LD}_{50}) + \gamma \cdot V_{\mathrm{Bio}} + \delta \cdot V_{\mathrm{Diver}} \tag{3}$$

Therein, weight parameters α, β, γ, δ were constrained such that $\alpha + \beta + \gamma + \delta = 1$, with each ≥ 0.1 to ensure balanced contributions.

All reactions were mapped into a four-dimensional feature space, from which Pareto-optimal candidates were extracted (Figure 7a red dots in “reactions score”). To determine the most balanced weight combination, a grid search was conducted over 885 feasible $(\alpha, \beta, \gamma, \delta)$ sets, with the objective of minimizing score variance across the Pareto front (see Section 5.3, Table S13). The optimal combination ($\alpha = 0.55$, $\beta = 0.1$, $\gamma = 0.1$, and $\delta = 0.25$, minimum variance $= 0.004$) was applied to evaluate all connected chains in the reaction network using depth-first search (DFS), as illustrated in the “paths evaluation” panel. For each predefined degradation pathway, the sequence with the highest cumulative score was selected as the optimal route (Figure 7b). Robustness was validated through sensitivity analysis across ten near-optimal weight combinations (Figures S26, S27), confirming that the identified routes remained largely consistent under moderate weight perturbations. This highlights the stability and generalizability of the DEBF scoring framework.

This framework enables identification of degradation pathways that are not only possible occurrence, low in toxicity, and biodegradation, but also topologically diverse, facilitating the search of more robust and novel degradation strategies.

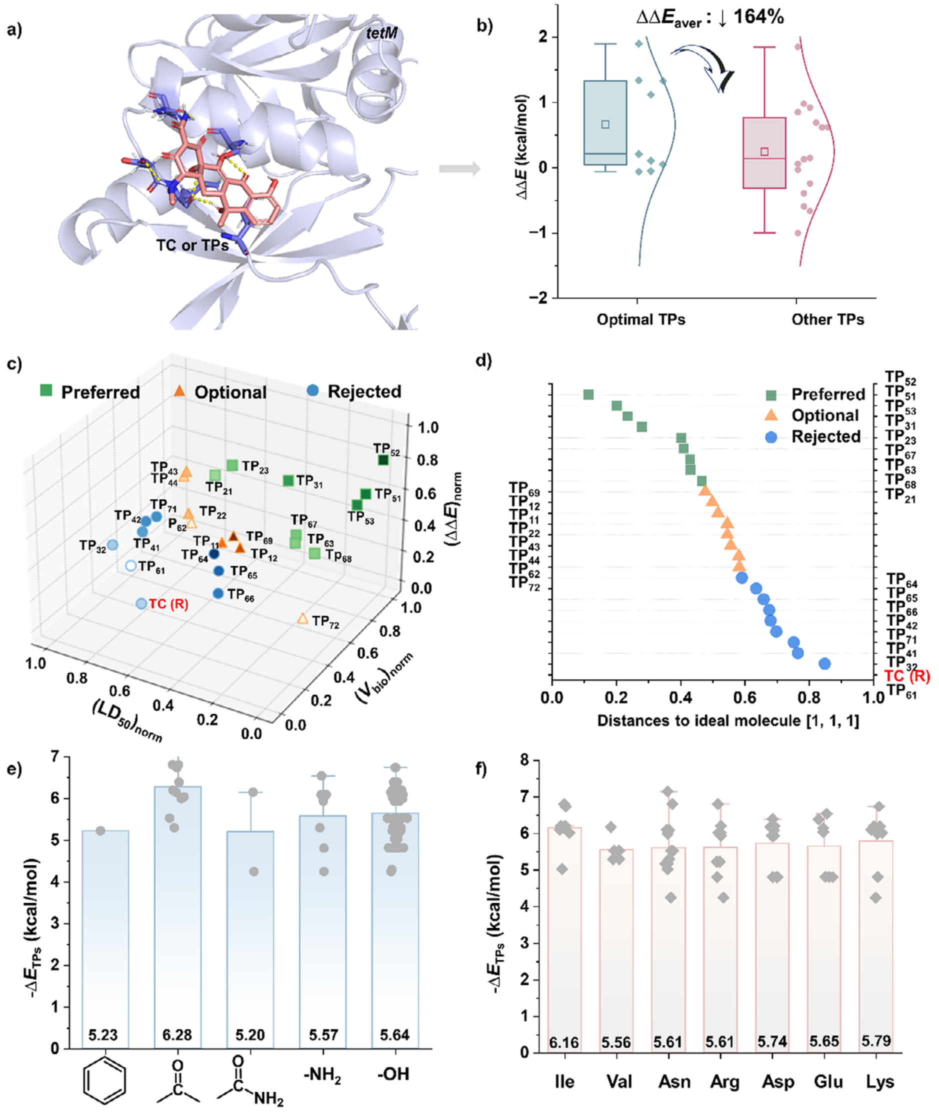

Figure 8. Antibiotic resistance risk induction evaluation of transformation products with *tetM*. a) Binding interaction between TC/TPs and *tetM*. b) Comparison of average $\Delta\Delta E$ between optimal TPs (from selected pathways) and other TPs. c) Three groups risk classification (low-risk (green squares, preferred molecules), medium-risk (orange triangles, optional molecules) and high-risk (blue circles, rejected molecules)) of TPs based on normalized toxicity, biodegradability, and $\Delta\Delta E$. d) 2D projection of ARG risk based on Euclidean distance to the ideal point (1, 1, 1). e) and f) Representative docking groups and residue interaction analysis between TPs and *tetM*, respectively.

Indeed, DEBF is applicable to provide a design−oriented evaluation that prioritizes environmentally preferable routes, if they are chemically and kinetically accessible, based on multi−criteria assessment. Such scoring supports informed decision−making in catalyst optimization and sustainable water treatment engineering. For example, routes producing TP_{32} was predicted to be highly toxic (LD_{50} = 471.51 mg kg^{-1}) and recalcitrant to biodegradation, and thus represent environmentally undesirable degradation outcomes.

Antibiotic Resistance Genes Binding Tendency of Transformation Products

ARGs have emerged as global environmental contaminants. Although balanced and eco-friendly degradation pathways were previously identified, the potential risk that residual TPs may still induce ARG expression or propagation remained to be evaluated. Here, we selected tetracycline resistant gene (*tetM*) (structure from AlphaFold Protein Structure Database[43]) as a representative ARG and conducted molecular docking simulations using Autodock.[44] The binding energies of TPs with *tetM* (ΔE_{TPs}) were evaluated to compare with the parent compound (ΔE_{TC}). To facilitate interpretation, the relative binding energies ($\Delta\Delta E = \Delta E_{TPs} - \Delta E_{TC}$) of TPs with *tetM* were classified into three categories: binding-enhanced ($\Delta\Delta E \leq -0.5$ kcal mol^{-1}), binding-retained (-0.5 kcal $mol^{-1} < \Delta\Delta E \leq 0.5$ kcal mol^{-1}), and binding-weakened ($\Delta\Delta E > 0.5$ kcal mol^{-1}) (see Table S14 for detailed classification criteria). As shown in Figures 8a and S28, some TPs (like TP_{61}, TP_{64}, and TP_{65}) exhibited similar or even stronger binding than TC, suggesting that these species may retain the potential to interact with ARG-related proteins. Notably, the products from the five optimal degradation pathways (optimal TPs) showed weaker binding affinities, with an average $\Delta\Delta E$ of 0.66 kcal mol^{-1}, representing a 1.64-fold reduction compared to other TPs (Figure 8b). This result supports the robustness and reliability of the systematic degradation pathway selection strategy.

A 3D feature space was constructed to quantify the resistance risk. The values of toxicity (LD_{50}), biodegradability (V_{Bio}), and $\Delta\Delta E$ were min–max normalized to follow a "larger is better" trend. Based on the total scores, the risks of TPs were classified into three groups, including low-risk, medium-risk, and high-risk. From Figure 8c (pairwise comparisons were seen in Figure S29), it was observed that most of optimal TPs belong to preferred molecules (as environmental-friendly). The classification was projected onto 2D space by computing Euclidean distances from the ideal point [1, 1, 1], representing low toxicity, high biodegradability and minimal binding tendency. Shorter distances indicate better performance, allowing a clear visual separation between preferred and rejected molecules (Figure 8d). Binding interaction analysis (Figures 8e and S30) revealed that TC and some TPs (e.g., TP_{61}, TP_{32}, and TP_{41}) commonly interact with *tetM* through polar groups (like hydroxyl, amide ketone and amine), forming hydrogen bonds (HBs) or electrostatic interactions with key residues. Residue-level analysis (Figure 8f and residue-level binding interactions in Table S15) showed that general TPs preferentially bind to key residues such as Ile339A, Lys337A, and Asp363A, while optimal TPs interact less frequently with these sites, indicating a reduced molecular interaction potential with resistance-associated targets.

Conclusion

In this study, we developed a mechanism-informed and risk-aware framework (DFT-ML) to systematically evaluate the photocatalytic degradation of representative antibiotics. Experimental analyses (EPR, LC–MS, HRMS and scavenger tests) confirmed the involvement of multiple ROS and revealed distinct transformation pathways. By integrating DFT calculations with electronic-structure-based reactivity profiling, atom-level degradation hotspots were identified, and site-selective radical attack mechanisms were elucidated.

A large-scale reaction database comprising 9 533 ΔG values enabled the ML models to accurately predict reaction energetics, significantly accelerating pathway screening. Furthermore, the multi-dimensional informative scoring system (DEBF) incorporating thermodynamic feasibility, toxicity, biodegradability, and structural diversity prioritized sustainable degradation routes. Molecular docking analyses demonstrated that TPs from the optimal pathways exhibited weakened binding to TC resistance gene *tetM*, suggesting a reduced possibility for resistance-related molecular interactions.

This integrated experimental–computational–machine learning approach not only provides atomistic insight into antibiotic degradation mechanisms but also establishes a robust decision framework for identifying eco-friendly and low-risk degradation pathways. These results advance the mechanistic understanding of photocatalytic antibiotic removal and offer a generalizable strategy for the design and assessment of sustainable pollutant transformation systems. Future efforts should benchmark its predictions against empirical ecotoxicological datasets and resistance gene expression assays to further validate its environmental relevance.

Supporting Information

Dataset, machine learning algorithms, experimental method, calculations, LC-MS and HRMS spectra, possible TPs and reactions during TC degradation, electronic parameters of TC, antibiotic structure–degradation site association model, toxicity and biodegradation prediction and protein docking details and results. The complete dataset (Tetracycline Degradation Dataset), including the reaction list, molecular descriptors (ML input features), DFT-calculated ΔG values, and the ML training code, is available for academic use in a public GitHub repository (https://github.com/zcc77a/Tetracycline-Degradation-Dataset).

Acknowledgements

Financial support for this work was provided by the National Key Research and Development Program of China (2023ZD0120700), the National Natural Science Foundation of China (grant no. 22033004, 22373049, 22336002, 22425603), the Natural Science Foundation of Jiangsu Province (BK20232012).

Conflict of Interests

The authors declare no conflict of interest.

Data Availability Statement

The data that support the findings of this study are openly available in github at [https://github.com/zcc77a/Tetracycline-Degradation-Dataset], reference number.[45]

Keywords: Environmental risk assessment • Photocatalysis • Thermodynamic feasibility • Transformation pathways • Workflow-based prediction

---

[1] J. Guo, Y. Wang, Y. Shang, K. Yin, L. Qian, B. Gao, Y. Li, X. D. Duan, X. Xu, *Proc. Natl. Acad. Sci. USA* **2024**, *121*, e2313387121, https://doi.org/10.1073/pnas.2313387121.

[2] J. Hu, Y. Liu, X. Zhang, Z. Chen, M. Tang, Y. Lyu, X. You, D. E. Helbling, W. Sun, *Water Res.* **2025**, *285*, 124145, https://doi.org/10.1016/j.watres.2025.124145.

[3] F. Li, P. Wang, T. Zhang, M. Li, S. Yue, S. Zhan, Y. Li, *Angew. Chem. Int. Ed.* **2023**, *62*, e202313298, https://doi.org/10.1002/anie.202313298.

[4] P. Loffler, B. I. Escher, C. Baduel, M. P. Virta, F. Y. Lai, *Environ. Sci. Technol.* **2023**, *57*, 9474–9494, https://doi.org/10.1021/acs.est.2c09854.

[5] H. Ren, F. Qi, A. Labidi, J. Zhao, H. Wang, Y. Xin, J. Luo, C. Wang, *App. Catal. B: Environ.* **2023**, *330*, 122587, https://doi.org/10.1016/j.apcatb.2023.122587.

[6] S. Li, X. Li, Y. Liu, P. Zhang, J. Zhang, B. Zhang, *Chin. J. Catal.* **2025**, *72*, 130–142, https://doi.org/10.1016/S1872-2067(25)64652-3.

[7] X. L. Wu, S. Liu, Y. Li, M. Yan, H. Lin, J. Chen, S. Liu, S. Wang, X. Duan, *Angew. Chem. Int. Ed.* **2023**, *62*, e202305639, https://doi.org/10.1002/anie.202305639.

[8] J. Dong, P. Li, X. Ji, Y. Kang, X. Yuan, J. Tang, B. Shen, H. Dong, H. Lyu, *J. Hazard. Mater.* **2023**, *451*, 131083, https://doi.org/10.1016/j.jhazmat.2023.131083.

[9] Y. Qian, L. Guan, Y. Ke, L. Wang, X. Wang, N. Yu, Q. Yu, S. Wei, J. Geng, *Water Res.* **2024**, *253*, 121299, https://doi.org/10.1016/j.watres.2024.121299.

[10] D. A. Boiko, K. S. Kozlov, J. V. Burykina, V. V. Ilyushenkova, V. P. Ananikov, *J. Am. Chem. Soc.* **2022**, *144*, 14590–14606, https://doi.org/10.1021/jacs.2c03631.

[11] G. Wu, Y. Qian, F. Fan, Z. Zhang, Y. Zhang, Q. Yu, X. Zhang, H. Ren, J. Geng, H. Liu, *Water Res.* **2023**, *235*, 119895, https://doi.org/10.1016/j.watres.2023.119895.

[12] Z. Dai, J. Xu, J. Guan, M. Feng, Y. Liu, C. Xing, X. Cai, S. Wang, L. Lian, H. Dong, J. Z. Ren, W. Shi, A. K. An, S. Zhong, X. Guan, *Environ. Sci. Technol.* **2025**, *59*, 15853.

[13] N. Yu, Y. Deng, X. Wang, W. Shi, D. Zhou, B. Pan, H. Yu, S. Wei, *Environ. Sci. Technol.* **2023**, *57*, 8335–8346, https://doi.org/10.1021/acs.est.2c07774.

[14] Y. Qian, Y. Ke, L. Wang, N. Yu, Y. He, Q. Yu, S. Wei, H. Ren, J. Geng, *Environ. Sci. Technol.* **2025**, *59*, 4153–4164, https://doi.org/10.1021/acs.est.4c13144.

[15] L. V. Tetering, S. Spies, D. K. Q. Wildeman, J. K. Houthuijs, R. E. van Outersterp, J. Martens, A. R. Wevers, S. D. Wishart, G. Berden, J. A. Oomens, *Commun. Chem.* **2024**, *7*, 30, https://doi.org/10.1038/s42004-024-01112-7.

[16] K. Wang, S. Zhang, X. Zhou, X. Yang, X. Li, Y. Wang, P. Fan, Y. Xiao, W. Sun, P. Zhang, W. Li, S. Huang, *Nat. Methods* **2024**, *21*, 92–101, https://doi.org/10.1038/s41592-023-02021-8.

[17] J. V. Burykina, A. D. Kobelev, N. S. Shlapakov, A. Y. Kostyukovich, A. N. Fakhrutdinov, B. König, V. P. Ananikov, *Angew. Chem. Int. Ed.* **2022**, *61*, e202116888, https://doi.org/10.1002/anie.202116888.

[18] Y. Chen, W. Ren, T. Ma, N. Ren, S. Wang, X. Duan, *Environ. Sci. Technol.* **2024**, *58*, 4844–4851, https://doi.org/10.1021/acs.est.3c06376.

[19] J. Qian, X. Zhang, Y. Jia, H. Xu, B. Pan, *Environ. Sci. Technol.* **2025**, *59*, 1060–1079, https://doi.org/10.1021/acs.est.4c10073.

[20] B. Ling, S. Yao, S. Ouyang, H. Bai, X. Zhai, C. Zhu, W. Li, J. Xie, *Angew. Chem. Int. Ed.* **2024**, *63*, e202405866 https://doi.org/10.1002/anie.202405866.

[21] X. Xue, H. Chen, Y. Xiong, R. Chen, M. Jiang, G. Fu, Z. Xi, X. L. Zhang, J. Ma, W. Fang, Z. Jin, *ACS Appl. Mater. Interfaces* **2021**, *13*, 4975–4983, https://doi.org/10.1021/acsami.0c17947.

[22] L. Luo, L. Fu, H. Liu, Y. Xu, J. Xing, C. R. Chang, D. Y. Yang, J. Tang, *Nat. Commun.* **2022**, *13*, 2930, https://doi.org/10.1038/s41467-022-30434-0.

[23] C. Wang, Z. Zhan, H. Liu, Y. Li, J. Wu, P. Sun, G. Shen, *Chem. Eng. J.* **2024**, *482*, 148906, https://doi.org/10.1016/j.cej.2024.148906.

[24] S. B. Beil, S. Bonnet, C. Casadevall, R. J. Detz, F. Eisenreich, S. D. Glover, C. Kerzig, L. Næsborg, S. Pullen, G. Storch, N. Wei, C. Zeymer, *JACS Au* **2024**, *4*, 2746.

[25] M. Yang, L. Yang, G. Wang, Y. Zhou, D. Xie, S. Li, *J. Chem. Theory Comput.* **2018**, *14*, 5787–5796 https://doi.org/10.1021/acs.jctc.8b00799.

[26] G. Li, G. Li, X. Liang, Y. Tian, J. Lu, X. Xu, X. Liu, J. Ma, S. Li, Y. Zhu, *Chem. Sci.* **2025**, *16*, 18642–18651.

[27] Z. Li, P. Chen, Z. Ni, L. Gao, Y. Zhao, R. Wang, C. Zhu, G. Wang, S. Li, *Nat. Commun.* **2025**, *16*, 735, https://doi.org/10.1038/s41467-025-56000-y.

[28] X. Y. Gao, Y. Xiao, Q. Peng, F. Yang, D. Li, G. Wang, Y. Qian, J. J. Feng, *Angew. Chem. Int. Ed.* **2025**, *64*, e202405222, https://doi.org/10.1002/anie.202513768.

[29] G. Li, Z. Li, L. Gao, S. Chen, G. Wang, S. Li, *Phys. Chem. Chem. Phys.* **2023**, *25*, 23696–23707, https://doi.org/10.1039/D3CP02443A.

[30] X. Su, G. Li, L. He, S. Chen, X. Yang, G. Wang, S. Li, *Nat. Commun.* **2024**, *15*, 7549, https://doi.org/10.1038/s41467-024-51997-0.

[31] X. Liu, D. Li, G. Li, M. Wei, S. Yuan, M. Yang, L. He, S. Chen, Z. Li, L. Gao, G. Wang, S. Li, *Nat. Commun.* **2025**, *16*, 5458, https://doi.org/10.1038/s41467-025-60674-9.

[32] M. Yang, S. Chen, D. Li, L. Gao, G. Wang, S. Li, *Adv. Sci. 12*, **2025**, e11395, https://doi.org/10.1002/advs.202511395.

[33] J. Cao, G. Li, G. Wang, L. Gao, S. Li, *Org. Biomol. Chem.* **2022**, *20*, 2857–2862, https://doi.org/10.1039/D2OB00453D.

[34] W. Zou, M. Yang, L. He, G. Wang, S. Li, *Chem. - Eur. J.* **2022**, *29*, e202203526.

[35] R. Staub, Y. Harabuchi, C. Seraphim, A. Varnek, S. Maeda, *J. Chem. Theory Comput.* **2025**, *22*, 422–440.

[36] G. Li, H. Ling, C. Su, Z. Liu, G. Wang, M. Yang, S. Li, **2025**, ChemRxiv preprint https://doi.org/10.26434/chemrxiv-2025-sm7f3.

[37] M. Samy, A. Tawfik, A. I. Osman, R. S. Abodlal, A. El-Dissouky, T. E. Khalil, E. El-Helow, M. G. Alalm, *ACS Omega* **2024**, *9*, 30963–30974, https://doi.org/10.1021/acsomega.4c04007.

[38] C. Lykos, S. Sioulas, I. Konstantinou, *Catalysts* **2023**, *13*, 254, https://doi.org/10.3390/catal13020254.

[39] M. Berkani, A. Smaali, Y. Kadmi, F. Almomani, Y. Vasseghian, N. Lakhdari, M. Alyane, *J. Hazard. Mater.* **2022**, *421*, 126719, https://doi.org/10.1016/j.jhazmat.2021.126719.

[40] J. Wang, M. Yuan, C. Li, B. Zhang, J. Zhu, X. Hao, H. Lu, Y. Ma, *J. Colloid Interface Sci.* **2022**, *612*, 536–549, https://doi.org/10.1016/j.jcis.2021.12.190.

[41] R. Ouyang, S. Curtarolo, E. Ahmetcik, M. Scheffler, L. M. Ghiringhelli, *Phys. Rev. Mater.* **2018**, *2*, 083802, https://doi.org/10.1103/PhysRevMaterials.2.083802.

[42] US E. P. A., *Estimation Programs Interface Suite™ for Microsoft® Windows*, v 4.11. United States Environmental Protection Agency, Washington, DC, USA **2012**.

[43] M. Varadi, S. Anyango, M. Deshpande, S. Nair, C. Natassia, G. Yordanova, D. Yuan, O. Stroe, G. Wood, A. Laydon, A. Žídek, T. Green, K. Tunyasuvunakool, S. Petersen, J. Jumper, E. Clancy, R. Green, A. Vora, M. Lutfi, M. Figurnov, A. Cowie, N. Hobbs, P. Kohli, G. Kleywegt, E. Birney, D. Hassabis, S. Velankar, *Nucleic Acids Res.* **2022**, *50*, D439–D444, https://doi.org/10.1093/nar/gkab1061.

[44] G. M. Morris, R. Huey, W. Lindstrom, M. F. Sanner, R. K. Belew, D. S. Goodsell, A. J. Olson, *J. Comput. Chem.* **2009**, *30*, 2785–2791, https://doi.org/10.1002/jcc.21256.

[45] C.-C. Zhao, Tetracycline-Degradation-Dataset, GitHub repository, **2026**, https://github.com/zcc77a/Tetracycline-Degradation-Dataset.

Manuscript received: September 12, 2025
Revised manuscript received: December 31, 2025
Manuscript accepted: January 04, 2026
Version of record online: January 20, 2026